Atomic-scale structural analysis by total scattering profiles

Masatsugu Yoshimoto*

Abstract

In the past, total scattering data was used to obtain the pair distribution function (PDF) $G(r)$. However, it has become clear that it is also possible to calculate characteristic values related to the physical properties of materials from the total scattering data. In this paper, we introduce two applications using total scattering data. The first evaluates the atomic density of materials using total scattering data. The atomic density of SiO_2 glass obtained by applying the proposed method is consistent within 5% of the literature value. The other is a new application of the Reverse Monte-Carlo (RMC) method for non-crystalline materials. It does not require any additional parameters to calculate diffraction peaks. The proposed method is used to identify specific features of the MnO_6 octahedra of the spinel lithium manganese oxide ($LiMn_2O_4$) corresponding to each Mn valence.

1. Introduction

For a long time, local structure analysis—the so-called the pair distribution function PDF method—has been widely used to understand local structure of non-crystalline materials (e.g., glasses and liquids). Since V. Petkov et al. reported the local structure of $Ga_{(1-x)}In_xAs$[1], it has also been used to analyze local structure in crystalline materials. After their work, PDF analysis of crystalline materials has been widely used in many material sciences fields (e.g., batteries[2, 3], catalysts[4], and ferroelectrics material[5]) for the following reasons: First, it is good to combine Rietveld analysis, which is widely used for crystal structure analysis, with the crystalline PDF analysis, which requires crystal structure information. Second, a laboratory system such as the SmartLab equipped with a high-energy target (Ag, Mo) can measure the total scattering intensity over a wide Q range. Detailed information on a laboratory system for total scattering measurements was included in our previous paper [6].

The PDF $G(r)$ is directly obtained from the Fourier transform of the experimental structure factor $S(Q)$. The information obtained from $G(r)$ is as follows: peak positions indicate the average distances between atoms, the peak widths note the distribution of neighbor atoms (crystallinity), and the peak areas indicate the coordination numbers. Coordination number calculation from $G(r)$ requires an accurate atomic number density for the material. However, it is sometimes difficult to determine this property if the material is porous and/or exists in a fine powder state that contains defects or voids.

In this article, we introduce two approaches using total scattering data. One is to evaluate the atomic density of materials from the total scattering data and the atomic composition of a material. The other is a new application of the Reverse Monte-Carlo (RMC) method for non-crystalline materials without using any additional parameters to calculate Bragg peak profiles.

* X-ray Research Laboratory, Rigaku Corporation.

2. Determining the Density of a Material from Total Scattering Data

2.1 Introduction

The density of a material is a basic physical property calculated from volume and weight. In the case of a perfect crystal, the density can be calculated from the atomic arrangement and volume of the unit cell. For example, the density of silicon ($\rho_0 = 0.049936$ atoms·Å$^{-3} = 2.32$ g/cm^3) calculated using the lattice parameter from NIST 640f (space group: $Fd\bar{3}m$, $a = 5.431144$ Å)[7] with 8 Si atoms in the unit cell is consistent with the bulk density. However, the material used in the actual model is a powder that contains various defects and pores between micro-scale and meso-scale; defects in the lattice, interparticle voids, pores in the structure, and roughness of the interface. The volume can only be evaluated by measuring the surface and quantifying pores that are accessible by the probe molecule; closed pores and defects in the atomic-scale structure cannot be measured. Therefore, to evaluate the physical property of a material, a method of estimating the atomic density independent of the sample state is needed.

It is well known that the density of a sample is closely related to $S(Q)$ and the total scattering intensity with absolute scale. Yevick G. J. and Percus J. K. reported that $S(Q)$ and $G(r)$ were described by only two parameters: the nearest neighbor distance and the packing fraction in the monatomic hard sphere case[8]. These results indicate that $S(Q)$ and $G(r)$ contain information about those fundamental parameters in non-crystalline states. Furthermore, Krogh-Moe J. and Norman N. reported that an integral over the total scattering intensity with absolute scale is related to the density of a sample material[9, 10]; this is well known as the Krogh-Moe–Norman method. However, it cannot be

applied to the calculation of the microscopic density of a sample because the normalization constant is determined by the volume and mass of the irradiated area; the latter is affected by microscopic pores.

It is also known that the density of a sample can be calculated from the slope of $G(r)$ in the region less than the nearest-neighbor distance[11, 12]. The obtained $G(r)$ is, however, often affected by non-physical modulation of the experimentally observed $S(Q)$ and does not show a linear slope in the less-than-nearest-neighbor region; therefore, the estimated density has a large uncertainty [12]. To overcome this problem, we have developed a Q-space iteration formula to remove such unphysical modulation of the experimentally observed $S(Q)$ without introducing any ambiguous parameters. Then, the corrected $G(r)$ satisfies the physical condition in the short-distance region, and we can reliably estimate the microscopic density.

2.2 Outline of the determination density

The observed structure factor $S_{obs}(Q)$ can be obtained from the coherent scattering intensity $I_{coh}(Q)$ as shown in Eq. (1):

$$S_{obs}(Q) = \frac{I_{coh}(Q) - \langle f^2 \rangle + \langle f \rangle^2}{\langle f \rangle^2}, \tag{1}$$

where $Q = 4\pi \sin(2\theta/2)/\lambda$, 2θ is the scattering angle and λ is the wavelength of the X-rays. $\langle f^2 \rangle$ and $\langle f \rangle$ are the mean squared average atomic scattering factor and the average atomic scattering factor, respectively, as defined in Eqs. (2.1) and (2.2):

$$\langle f \rangle = \sum_i c_i f_i, \tag{2.1}$$

$$\langle f^2 \rangle = \sum_i c_i f_i^2, \tag{2.2}$$

where c_i and f_i are the atomic concentration and atomic form factor for the ith types of atoms, respectively. The observed PDF, $G_{obs}(r)$, can be calculated from the Fourier transform of $S_{obs}(Q)$ as shown in Eq. (3):

$$G_{obs}(r) = \frac{2}{\pi} \int_0^\infty Q\{S_{obs}(Q) - 1\} \sin Qr \, dQ. \tag{3}$$

According to its physical meaning, $G(r)$ can be written in terms of the local atomic density $\rho(r)$ and the average density ρ_0, as:

$$G_{obs}(r) = 4\pi r(\rho(r) - \rho_0) \tag{4}$$

In the region less than the interatomic distance, r_{min}, there must be no atoms; therefore, $\rho(r) = 0$ where $r \le r_{min}$. Then, the ideal $G_I(r)$ should satisfy the following equation in this region[11, 12],

$$G_I(r \le r_{min}) = -4\pi r \rho_0. \tag{5}$$

In general, the observed structure factor $S_{obs}(Q)$ may include non-physical modulations over the wide Q range due to experimental errors, and thus the experimental $G_{obs}(r)$ does not satisfy the condition in Eq. (5). In this case, the structure factor can be corrected by assuming it should be consistent with Eq. (5) and obtained by replacing the observed $G_{obs}(r)$ with the ideal $G_I(r)$ in the range of $r \le r_{min}$,

$$\begin{aligned} S_{cor}(Q) - 1 = &\int_0^\infty G_{obs}(r) \frac{\sin Qr}{Q} dr \\ &- \int_0^{r_{min}} G_{obs}(r) \frac{\sin Qr}{Q} dr \\ &+ \int_0^{r_{min}} G_I(r) \frac{\sin Qr}{Q} dr. \end{aligned} \tag{6}$$

When we define the new two functions, $\alpha(Q)$ and $\beta(Q)$, as:

$$\alpha(Q) = \int_0^{r_{min}} -4\pi r \frac{\sin Qr}{Q} dr, \tag{7.1}$$

$$\beta(Q) = \int_0^{r_{min}} G_{obs}(r) \frac{\sin Qr}{Q} dr, \tag{7.2}$$

Eq. (6) can be written as follows:

$$S_{cor}(Q) = S_{obs}(Q) - \beta(Q) + \rho_0 \alpha(Q) \tag{8}$$

In Eq. (8), the number density ρ_0 is treated as a scale factor that minimizes the residual sum of squares (RSS) between $\rho_0 \alpha(Q)$ and $\beta(Q)$. Then, ρ_0 is derived as follows:

$$\rho_0 = \frac{\sum_i (\alpha(Q_i)\beta(Q_i))}{\sum_i (\alpha(Q_i)^2)}. \tag{9}$$

This procedure is applied repeatedly j times, as shown in Fig. 1, until the residual R_j (%), defined as:

$$R_j(\%) = \sqrt{\frac{(\rho_0(j-1) - \rho_0(j))^2}{\rho_0(j)^2}} \times 100 \tag{10}$$

becomes close to zero. Finally, we can estimate the average density ρ_0 of a material.

2.3 Experimental section

To verify our method for determining the density ρ_0, we performed a total scattering measurement for SiO_2 glass using a SmartLab (Rigaku Corp.) equipped with a high-speed 1D detector. The incident X-rays were monochromatized by a focusing multilayer mirror, and the obtained X-ray energy was $E_{Ag\ K\alpha} = 22.11$ keV. The total scattering measurement was done with the scattering angle 2θ and its corresponding scattering vector Q ranging from 2.4° and 0.47 Å^{-1} to 157° and 21.958 Å^{-1}, respectively. A rod-shaped SiO_2 glass, whose diameter is 0.5 mm and length 80 mm, was

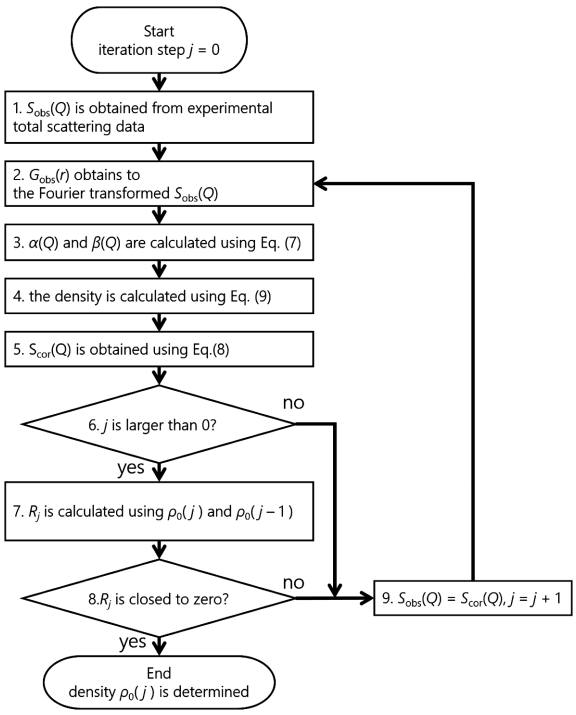

Fig. 1. The scheme for the determination of density from total scattering data.

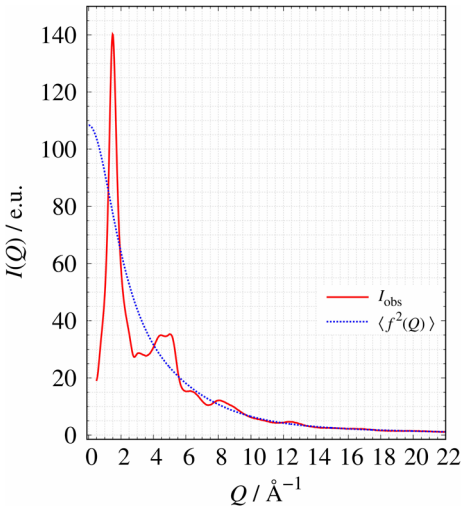

Fig. 2. The coherent scattering intensity (red solid line) and the atomic scattering factor (blue broken line) of SiO_2 glass.

purchased from Nakahara Opto-Electric Lab., Inc. The coherent scattering intensity $I_{coh}(Q)$ of SiO_2 glass was obtained using the established correction procedures[6].

2.4 Results and discussion

The collected scattering intensity $I_{coh}(Q)$ oscillates symmetrically around the mean squared average of $\langle f^2 \rangle$ over the entire Q range and the PDF analysis could be performed correctly as shown in Fig. 2.

Figure 3a shows $S_{obs}(Q)$, $S_{cor}(Q)$, and the residual curve between them. The residual curve does not contain structural information. It is mainly caused by two

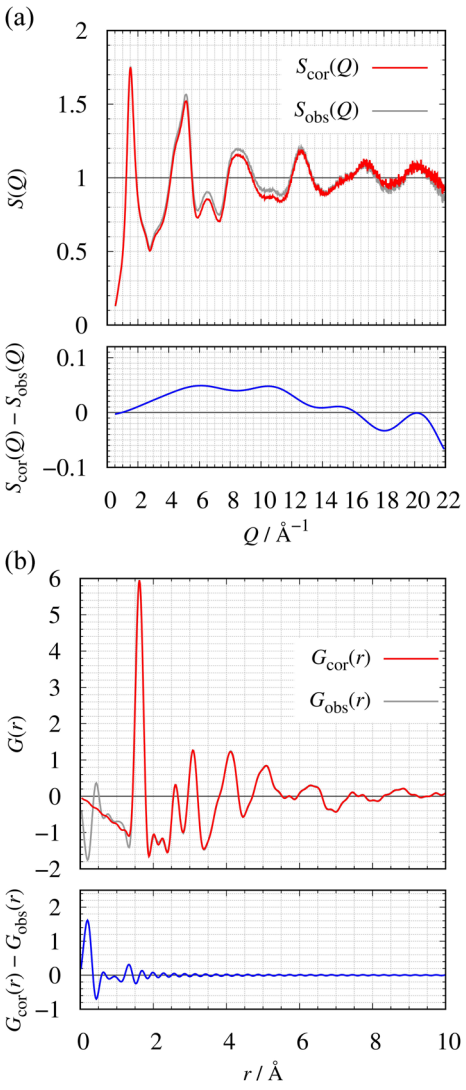

Fig. 3. (a) Comparison of $S(Q)$ before (gray), after correction (red) and the residual curve between them (blue). (b) The corresponding $G(r)$.

factors: incoherent Compton scattering and background scattering from the sample container[12]. Figure 3b shows $G_{obs}(r)$, $G_{cor}(r)$, and their difference. The corrected $G_{cor}(r)$ satisfies the condition Eq. (5) after eliminating the non-physical modulation from $G_{obs}(r)$ in the range of $r < 1.3$ Å, and a reliable average density ρ_0 is obtained by applying Eq. (9).

Figure 4a shows the iterated procedure of ρ_0, which converged to $\rho_0 = 0.06311$ atoms·Å^{-3} as the number of iterations increased. The R-value gradually decreases for each iteration step as shown in Fig. 4b. The determined SiO_2 glass number density ($\rho_0 = 0.06311$ atoms·Å^{-3}) coincides with the reported bulk density ($\rho_{bulk} = 0.06613$ atoms·Å^{-3}) within ±5%[13), (14)].

We also validated the Q range dependency of the determined value. The determined density is $\rho_0 = 0.06969$ atoms·Å^{-3} calculated from the total scattering intensity measured by Mo Kα ($\lambda = 0.7107$ Å, $E_{MoK\alpha} = 17.45$ keV) and is in good agreement with that using Ag Kα ($\lambda = 0.5608$ Å, $E_{Ag\ K\alpha} = 22.11$ keV).

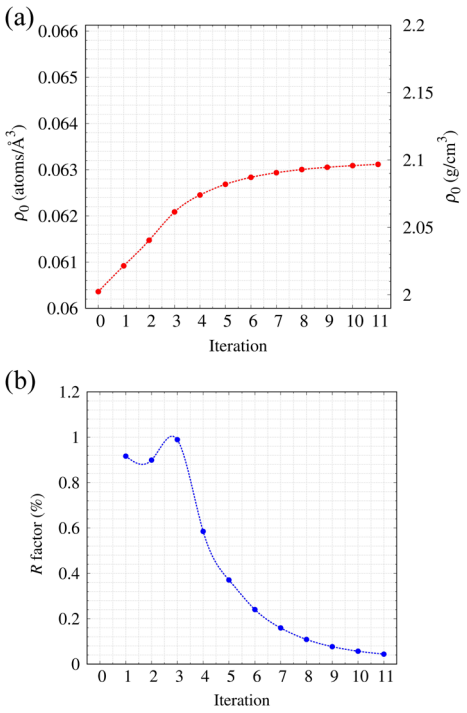

Fig. 4. (a) The atomic number density after each iteration. (b) The corresponding *R*-factor.

The proposed method can estimate the appropriate density using total scattering intensity measured by high-energy X-rays such as Ag Kα and Mo Kα, but it is not suitable for calculating the density using relatively long wavelength X-rays like Cu Kα ($\lambda = 1.5423$ Å, $E_{\mathrm{Cu\,K}\alpha} = 8.04$ keV). This is because $G_{\mathrm{obs}}(r)$ must be convoluted with the termination error arising from the measurable maximum Q value, Q_{max}. Moreover, the minimum peak width of $G_{\mathrm{obs}}(r)$ is determined by the termination error and broadens with decreasing Q_{max} value. The determined density contains a large error because the effect of termination error cannot be ignored when the X-ray wavelength is longer than that of Ag Kα and Mo Kα radiation.

2.5 Conclusion

The proposed method only requires the nearest-neighbor distance, which can be estimated from the coherent scattering intensity of a material as shown in Fig. 2, without any unphysical assumptions. In other words, only the reliable total scattering intensity and the atomic composition ratio of a material are required. The proposed method can be widely applied to any crystalline or amorphous material containing defects and pores in its structure. Detailed information about density determination and further applications can be found in Ref. 15.

3. A New Approach to the Local Structure in a Crystalline Material

3.1 Introduction

The properties of a novel material are related to not only the average structure but also the disordered local structure; for example, the particle size dependence of permittivity of $BaTiO_3$[5), (16), (17)] and Li-ion diffusion in solid electrolytes[(18)–(20)]. It is also well known that the materials for Li-ion batteries undergo structural changes during charge and discharge reactions. Several studies have demonstrated that the graphite structure changes upon intercalation of Li atom using X-ray diffraction[(21)–(23)] and Raman spectroscopy[(24)], and that the lattice parameter for the cathode material changes during Li insertion and extraction according to X-ray diffraction profiles[(25)].

The spinel $LiMn_2O_4$ (LMO) is one of the most famous cathode materials because of its thermal stability, non-toxicity, and low production cost[(26)]. LMO has a structural phase transition[(27), (28)] with a hysteresis between the heating and cooling processes[(29), (30)]. In the high-temperature phase, LMO forms a cubic structure with space group $Fd\bar{3}m$. There is one unique MnO_6 octahedra in cubic spinel LMO. In the low-temperature phase, the spinel LMO forms an orthorhombic structure that is a $3a \times 3a \times 1a$ superstructure based on the cubic spinel LMO, with space group *Fddd*. In the low-temperature phase, the MnO_6 octahedra are distorted and separated into five types. It has been suggested that some of the MnO_6 octahedra form $Mn^{3+}O_6$ and are distorted as a result of the Jahn-Teller effect[(27), (30), (31)].

The Reverse Monte Carlo RMC method developed by R. L. Mcgreey and L. Putzai[(32)] directly searches the optimized coordination of individual atoms consistent with the experimental total scattering data, making it suitable for the study of disordered local structure in crystalline materials. For crystalline materials, local structure estimation using $G_{\mathrm{obs}}(r)$ and $S_{\mathrm{obs}}(Q)$ each face different technical problems. In the case of $G_{\mathrm{obs}}(r)$, the direct comparison of $G_{\mathrm{obs}}(r)$ and $G_{\mathrm{RMC}}(r)$ may suffer from artifacts in the estimated structure because structural deformations in a crystalline material can be small compared with the termination error arising from the measurable maximum Q value Q_{max}. To solve this problem, it is proposed to use $G'_{\mathrm{RMC}}(r)$, which is $G_{\mathrm{RMC}}(r)$ convoluted with the termination error, to estimate the local structure[(33)]. In the case of $S_{\mathrm{obs}}(Q)$, the dimension of the calculation box (simulation box) is too small to calculate the diffraction peaks correctly. The first attempt at a local structure study for a crystalline material comparing the results of the RMC method with the experimental structure factor $S(Q)$ was reported by V. M. Nield et al.[(34)] Their method is an interesting approach but has a problem in that the original structure factor $S(Q)$ has been changed by convolution with the simulation box size effect. Therefore, the modified structure factor includes an artificial fringe due to the termination error caused by ending the calculation at a finite distance. The amplitude of the fringe is comparable to that from the real structure of materials, making it difficult to judge the validity of the simulated results.

At the present time, we have found two major approaches for modeling the local structure in a crystalline material including the calculation of

diffraction peaks. One is the RMCPOW program developed by A. Mellergard and R.L. McGreevy[35, 36], which directly calculates the diffraction intensities from an average structure and the diffuse intensity from a disordered local structure using the atomic arrangement derived from RMC calculations. RMCPOW, however, has some limitations: there is a high calculation cost because it requires a large simulation box, and it requires the Q-resolution function of the experimental instrument to calculate sharp diffraction peak profiles. The other program is RMCProfile, developed by M. G. Tucker et al. It also separately calculates scattering intensity coming from the local structure and periodic crystalline structure[37, 38]. The former is calculated from the radial distribution functions obtained from the RMC and the latter is calculated using the Bragg peak profile function. These two approaches require additional parameters to simulate diffraction peak profiles to obtain reliable fitting between the model structure and the observed experimental data. Therefore, if we use these two methods, the diffraction peak calculations would be affected by ambiguous parameters. To avoid the need for such additional parameters and to simplify the RMC procedure, we have proposed a method to reproduce the experimental total scattering pattern based on the simulated local structure without introducing any ambiguous parameters.

In this article, we explain the procedure of the proposed RMC method and then demonstrate the advantages of the proposed method using crystalline Ni data and the structural model. Next, we discuss the local structure of spinel LMO.

3.2 Outline of the estimation of the local structure of crystalline materials

It is important to note that, in this article, "*local structure*" means the correlation calculated from the atomic arrangements put in the simulation box and "*periodic structure*" means the long-distance correlations corresponding to the periodic crystalline structure outside the simulation box.

The observed pair distribution function $G_{\mathrm{obs}}(r)$ is directly obtained from the Fourier transform of the observed structure factor ($F(Q) = S(Q) - 1$) as follows:

$$G_{\mathrm{obs}}(r) = 4\pi r\rho_0\{g(r)-1\} = \frac{2}{\pi}\int_{Q_{\min}}^{Q_{\max}} QF_{\mathrm{obs}}(Q)\sin Qr\, dQ. \quad (11)$$

where ρ_0 is the average number density of a material, $g(r)$ is the pair distribution function, and Q is the scattering vector. The task of the RMC approach is to reproduce a three-dimensional local structure consistent with the observed $S_{\mathrm{obs}}(Q)$ satisfying Eq. (11). We assume $F(Q)$ can be separated into two terms as follows:

$$F(Q) = F^L(Q) + F^P(Q), = \int_0^{r_{\max}} 4\pi r^2\rho_0\left(g(r)-1\right)\frac{\sin Qr}{Qr}dr + \int_{r_{\max}}^{\infty} 4\pi r^2\rho_0\left(g(r)-1\right)\frac{\sin Qr}{Qr}dr, \quad (12)$$

where $F^L(Q)$ is the local structure term, $F^P(Q)$ is the long-range periodic structure term and $r_{\max}$ is the maximum distance of the RMC calculation.

Generally, we can obtain only $F^L(Q)$ because the RMC simulation must be performed with a realistic finite box size. Therefore, unphysical termination fringes were noticed. To avoid such unphysical fringes, we have added a long-range periodic part $F^{\mathrm{P}}(Q)$, which is calculated from the experimental pair distribution function:

$$F^{\mathrm{P}}_{\mathrm{obs}}(Q) = \int_{r_{\max}}^{\infty} 4\pi r^2\rho_0\left(g_{\mathrm{obs}}(r)-1\right)\frac{\sin Qr}{Qr}dr. \quad (13)$$

Then, we can obtain the following calculated structure factor:

$$F_{\mathrm{RMC}}(Q) = F^{\mathrm{L}}_{\mathrm{RMC}}(Q) + F^{\mathrm{P}}_{\mathrm{obs}}(Q). \quad (14)$$

$F^{\mathrm{L}}_{\mathrm{RMC}}(Q)$ is obtained from the Fourier transform of the pair distribution function $g_{\mathrm{RMC}}(r)$, which is calculated from the atomic configuration in the calculation box:

$$F^{\mathrm{L}}_{\mathrm{RMC}}(Q) = \int_0^{r_{\max}} 4\pi r^2\rho_0\left(g_{\mathrm{RMC}}(r)-1\right)\frac{\sin Qr}{Qr}dr. \quad (15)$$

The calculated structure factor $F_{\mathrm{cal}}(Q)$ obtained by Eqs. (14) and (15) is optimized via the RMC procedure to satisfy

$$F_{\mathrm{RMC}}(Q) = F_{\mathrm{obs}}(Q). \quad (16)$$

The calculation error is estimated as:

$$R_{\mathrm{p}} = \sqrt{\frac{\sum_i^n\left(S_{\mathrm{obs}}(Q_i) - S_{\mathrm{RMC}}(Q_i)\right)^2}{\sum_i^n S^2_{\mathrm{obs}}(Q_i)}}. \quad (17)$$

RMC trials are performed to decrease R_{p} by changing the atomic configuration in the simulation box until R_{p} becomes almost constant.

Figure 5 shows that the local structure term $F^{\mathrm{L}}_{\mathrm{obs}}(Q)$ and the periodic structure term $F^{\mathrm{P}}_{\mathrm{obs}}(Q)$ are separated from the observed structure factor $F_{\mathrm{obs}}(Q)$, which is obtained from a crystalline Ni powder and is applied to Eq. (12). In the low-Q region (until $r_{\max}$), both $F^{\mathrm{L}}_{\mathrm{obs}}(Q)$ and $F^{\mathrm{P}}_{\mathrm{obs}}(Q)$ contain a fringe caused by integration, and the fringes of $F^{\mathrm{L}}_{\mathrm{obs}}(Q)$ and $F^{\mathrm{P}}_{\mathrm{obs}}(Q)$ are in antiphase. The outline of the proposed RMC for a crystalline material was explained with $F(Q)$, but the actual structure is evaluated by using the structure factor $S(Q)$ ($= F(Q) + 1$).

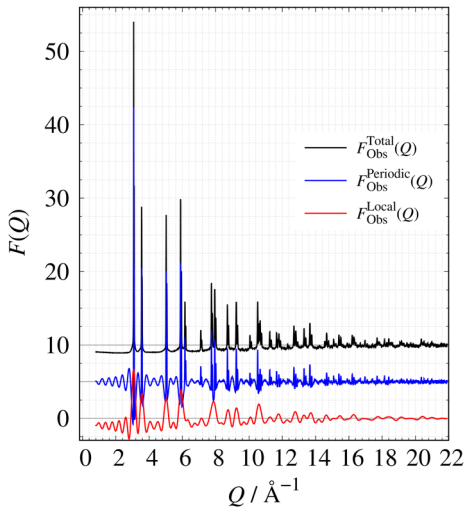

Fig. 5. An example of "*the local term*" $F^{L}_{obs}(Q)$ and "*the periodic term*" $F^{P}_{obs}(Q)$ separated from the observed $S_{obs}(Q)$ of crystalline Ni at a maximum distance $r_{max} = 20.0$ Å.

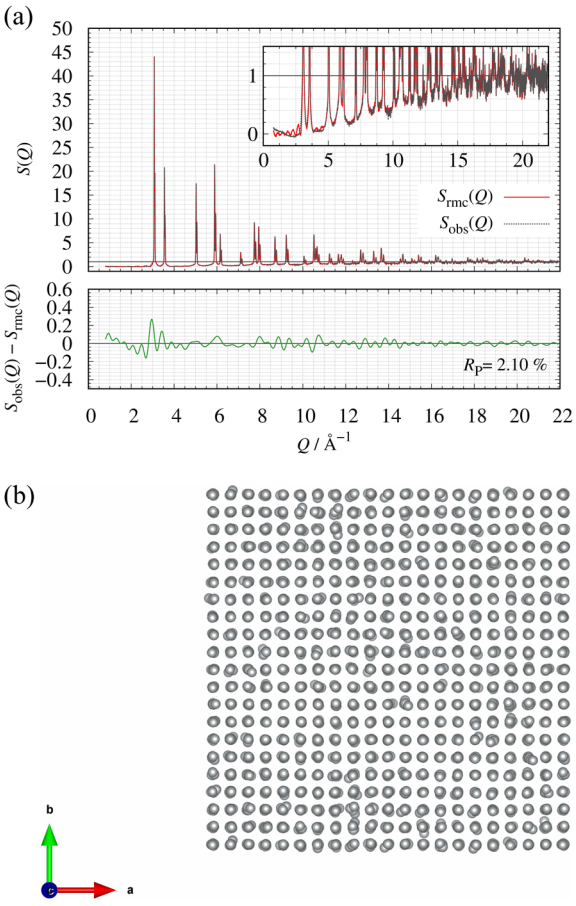

Fig. 6. The RMC modeling results of crystalline Ni. (a) Structure factors $S(Q)$: the calculated structure factor $S_{RMC}(Q)$ (red solid line), the observed structure factor $S_{obs}(Q)$ (gray broken line), and the residual curve between $S_{obs}(Q)$ and $S_{RMC}(Q)$ (green solid line), (b) The estimated structural model of Ni.

The Ni local structure is estimated using the proposed RMC starting from the initial atomic arrangement of $10 \times 10 \times 10$ Ni unit cells (space group: $Fd\bar{3}m$, lattice parameter: $a = 3.52503$ Å). Figure 6 shows the structure factor and the structural model after RMC calculation. The estimated structural model is visualized with the computer program *VESTA*[39]. The estimated local structural model of crystalline Ni is consistent with the $S_{obs}(Q)$ without introducing any ambiguous parameters as indicated by the low R-factor value, $R_p = 2.10\%$. Figure 7 shows the histogram of the atomic displacements calculated from the changes of atomic arrangements before and after RMC calculations. The root mean square (RMS) of the displacement distance is $\sigma = 0.0920$ Å, which is consistent with the atomic displacement parameter $\sigma = 0.0756$ Å obtained from the Rietveld analysis result. The local structure in crystalline Ni is represented by the displacement of atoms from their lattice points at a finite temperature. This indicates that the proposed RMC method can estimate the local structure in a crystalline material.

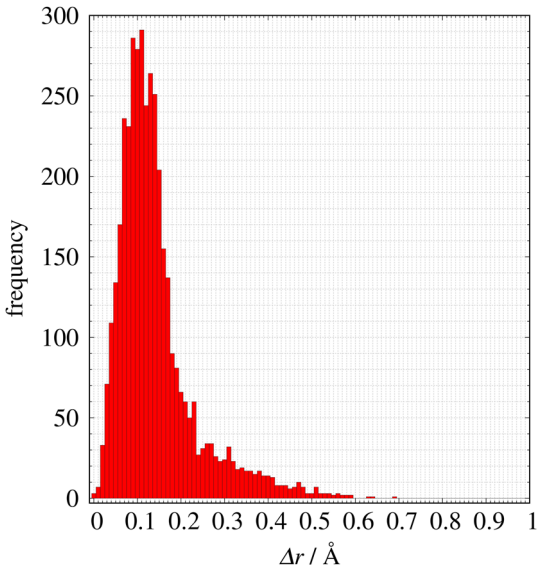

Fig. 7. The displacement histogram of Ni atom calculated from the atomic coordination before and after RMC calculation.

3.3 Experimental section

3.3.1 Total scattering measurement

The spinel LMO supplied by Toshima Manufacturing Co., Ltd. was sealed in a glass capillary with a diameter of 0.7 mm. Scattering from the blank capillary was measured as a background profile. We performed a total scattering measurement using a SmartLab (Rigaku Corp.) equipped with a high-speed 1D detector (D/teX HE). The incident X-rays were monochromatized by a focusing multilayer mirror, and the obtained X-ray energy was $E_{Ag\ K\alpha} = 22.11$ keV. The total scattering measurement was done with the scattering angle 2θ and its corresponding scattering vector Q ranging from 2.4° and 0.47 Å^{-1} to 157° and 21.958 Å^{-1}, respectively. The structure factor $S_{obs}(Q)$ and the PDF $G_{obs}(r)$ were obtained using established correction procedure[6].

Table 1. The atomic coordination of cubic spinel-$LiMn_2O_4$ ($Fd\bar{3}m$, Origin Choice 2, $a = 8.24352$ Å).

Atom	x	y	z	Site	Occupancy
Li	7/8	7/8	7/8	8a	1.0
Mn	1/2	1/2	1/2	16d	1.0
O	0.2626	0.2626	0.2626	32e	1.0

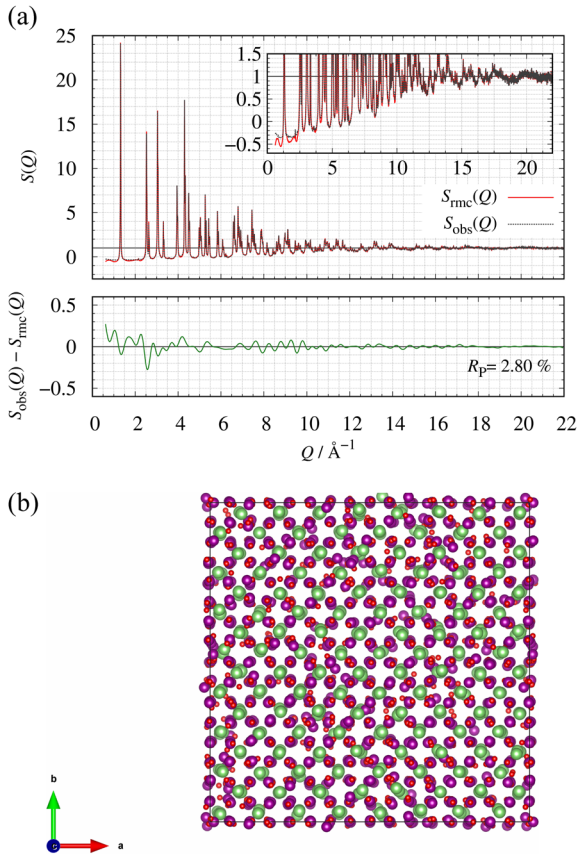

Fig. 8. The RMC modeling results of spinel LMO. (a) Structure factors $S(Q)$: $S_{RMC}(Q)$ (red solid line), $S_{obs}(Q)$ (gray broken line), and the residual curve between $S_{obs}(Q)$ and $S_{RMC}(Q)$ (green solid line), (b) The estimated structural model of LMO (Mn (violet), O (red), Li (green–yellow)). The displayed scale for each atom applies the atomic radius.

3.3.2 RMC calculation

To evaluate the distortion of the MnO_6 octahedra in the spinel LMO, RMC was performed using an initial atomic arrangement obtained from $4a \times 4$ $a \times 4a$ unit cells of the cubic spinel LMO whose lattice parameter was determined by Rietveld refinement as shown in Table 1. Trial moves whose magnitudes were at most $\Delta r = 0.1$ Å were generated for each MC step. The obtained structural model was visualized with the computer program *VESTA*[39].

3.4 Results and discussion

There is good agreement between the observed structure factor $S_{obs}(Q)$ and the calculated structure factor $S_{RMC}(Q)$ (Fig. 8a) as indicated by $R_p = 2.80\%$. Figure 8b also shows the estimated structural model of the spinel LMO. To characterize the valence of each simulated MnO_6 octahedra, the valence of all Mn atoms was evaluated using the bond valence sum (BVS) method, with parameters $r_0 = 1.75$ Å and $B = 0.374$ Å for the Mn–O bond[40].

$$BV = \sum_{i=1}^{n} \exp\left(\frac{r_0 - r_i}{B}\right), \tag{18.1}$$

where BV is the bond valence sum, n is the number of nearest bonds, r_0 is the parameter for the bond, r_i is the distance of the bond, and B is the bond valence

Table 2. The Mn valences, percentage, and the distortion parameter $\bar{\Delta}_{val}$ of each Mn valence for $4 \times 4 \times 4$ calculation box.

Valence	Percentage (%)	Distortion parameter, $\bar{\Delta}_{val}$ ($\times 10^{-4}$)
Mn^{2+}	5.56	228.76
Mn^{3+}	58.30	107.15
Mn^{4+}	35.74	46.13
Mn^{5+}	0.4	24.38

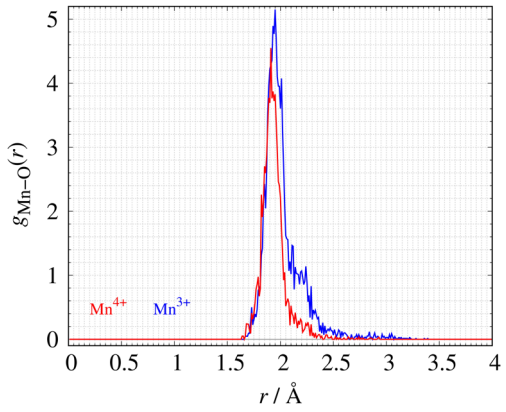

Fig. 9. The Mn^{n+}–O pair distribution function $g(r)$ of the MnO_6 octahedra for each Mn valence: Mn^{3+} (blue), Mn^{4+} (red)

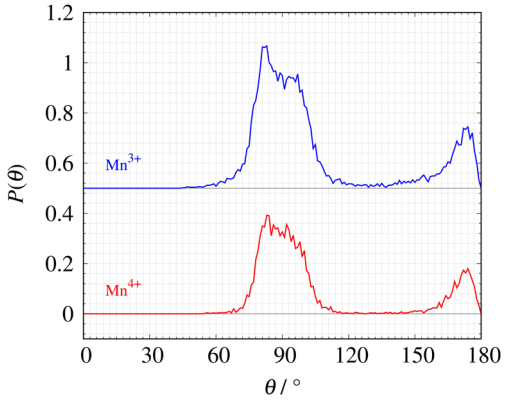

Fig. 10. The O–(Mn^{n+})–O angular histogram of the MnO_6 octahedra for each Mn valence: Mn^{3+} (blue), Mn^{4+} (red).

parameter.

The results are listed in Table 2. The average valence of the Mn sites is +3.3, which is lower than that of the Mn site calculated for the cubic spinel LMO (+3.5). This indicates that the number of Mn^{3+} atoms is larger than that of Mn^{4+} in the low temperature LMO. The correlations related to Mn^{+2} and Mn^{+5} are not used for detailed discussion of MnO_6 octahedra because those percentages (Mn^{+2}: 5.56% and Mn^{+5}: 0.4%) are very low.

Figure 9 shows $g_{Mn-O}(r)$ for each Mn atom valence. The average bond length of Mn^{3+}–O and the associated standard deviation σ are 2.05 Å and 0.0784 Å, respectively. On the other hand, the average bond length of Mn^{4+}–O and the associated standard deviation σ are 1.94 Å and 0.0294 Å, respectively. These results indicate that the Mn^{3+}–O bond is longer and has a wider distribution compared to Mn^{4+}–O. Figure 10 shows the angular histogram of O–Mn^{n+}–O for each Mn atom valence. The angular histogram of the ideal octahedra shows a peak at 90°, but the simulated Mn^{3+} angular histogram shows a peak at less than 90° and a wider distribution than that of Mn^{4+}. We also define the average distortion parameter of MnO_6 octahedra $\bar{\Delta}_{Val}$ for each Mn valence as:

$$\bar{\Delta}_{Val} = \frac{1}{n_{val}} \sum_{j=1}^{n} \Delta_j , \qquad (18.2)$$

where n_{val} is the number of each valence Mn atom categorized by the BVS analysis and Δ_j is the distortion parameter for each MnO_6 octahedra[27]. Table 2 also shows the average distortion $\bar{\Delta}_{Val}$ for each Mn valence. The $Mn^{3+}O_6$ octahedra are more distorted and show 2.3 times larger $\bar{\Delta}_{3+}$ than that of $Mn^{4+}O_6$ octahedra. We have also performed RMC simulation using the estimated structural model of $3a \times 3a \times 3a$ unit cell and obtained similar quantitative results, indicating that the present results have little dependence on the simulation box size when the size of the simulation box is sufficiently large. According to the results above, the present RMC procedure for disordered crystal materials is very useful to study small structural change, such as the Jahn-Teller effect reported in previous studies[27), (31), (41)].

3.5 Conclusion

The presented RMC approach based on total scattering data can be applied to study precise local structural changes in a crystalline material, such as the low-temperature phase of spinel LMO.

To correctly evaluate the local structure in a crystalline material using the RMC method, the initial atomic arrangement is obtained from a crystalline structure searched from the database and, at a minimum, the lattice parameter should be refined against the experimental total scattering data using the Rietveld method. In general, RMC is performed under the constraint that the volume of the calculation box and the numbers of atoms are constant. The RMC only provides a structural model consistent with the experimental total scattering data. Therefore, other properties of a material (i.e., the density and atomic concentration) should be determined using another measurement method.

The RMC method is useful to evaluate the local structure in a crystalline material. However, RMC, which is widely used around the world, has been a tool rarely used by general users because it is difficult to choose appropriate values for the parameters. On the contrary, our approach can be easily used by general users because there is no need to set ambiguous parameters, such as the instrument constant. In the near future, we will add the proposed RMC to the PDF plugin.

Reference

1) V. Petkov, I.-K. Jeong, J. S. Chung, M. F. Thorpe, S. Kycia, and S. J. L. Billinge: *Phys. Rev. Lett.*, **83** (1999) 4089–4092.
2) J. M. Stratford, M. Mayo, P. K. Allan, O. Pecher, O. J. Borkiewicz, K. M. Wiaderek, K. W. Chapman, C. J. Pickard, A. J. Morris, and C. P. Grey: *J. Am. Chem. Soc.*, **139**(2017), 7273–7286.
3) K. Ohara, A. Mitsui, M. Mori, Y. Onodera, S. Shiotani, Y. Koyama, Y. Orikasa, M. Murakami, K. Shimoda, K. Mori, T. Fukunaga, H. Arai, Y. Uchimoto, and Z. Ogumi: *Sci. Rep.*, **6**(2016), 21302.
4) M. Harada, R. Ikegami, L. S. R. Kumara, S. Kohara, and O. Sakata: *RSC Adv.*, **9**(2019), 29511–29521.
5) M. B. Smith, K. Page, T. Siegrist, P. L. Redmond, E. C. Walter, R. Seshadri, L. E. Brus, and M. L. Steigerwald: *J. Am. Chem. Soc.*, **130**(2008), 6955–6963.
6) Y. Shiramata and M. Yoshimoto: *Rigaku Journal*, **50**(2019), 1–8.
7) https://www-s.nist.gov/srmors/view_cert.cfm?srm = 640f
8) J. K. Percus and G. J. Yevick: *Phys. Rev.*, **110**(1958), 1–13.
9) J. Krogh-Moe: *Acta Cryst.*, **9**(1956), 951–953.
10) N. Norman: *Acta Cryst.*, **10**(1957), 370–373.
11) P. F. Peterson, D. Olds, M. T. McDonnell, and K. Page: *J. Appl. Cryst.*, **54**(2021), 317–332.
12) P. F. Peterson, E. S. Božin, T. Proffen, and S. J. L. Billinge: *J. Appl. Cryst.*, **36**(2003), 53–64.
13) P. Vashishta, R. K. Kalia, J. P. Rino, and I. Ebbsjö: *Phys. Rev. B.*, **41**(1990), 12197–12209.
14) Y. Onodera, S. Kohara, P. S. Salmon, A. Hirata, N. Nishiyama, S. Kitani, A. Zeidler, M. Shiga, A. Masuno, H. Inoue, S. Tahara, A. Polidori, H. E. Fischer, T. Mori, S. Kojima, H. Kawaji, A. I. Kolesnikov, M. B. Stone, M. G. Tucker, M. T. McDonnell, A. C. Hannon, Y. Hiraoka, I. Obayashi, T. Nakamura, J. Akola, Y. Fujii, K. Ohara, T. Taniguchi, and O. Sakata: *NPG Asia Mater.*, **12**(2020), 85.
15) M. Yoshimoto and K. Omote: *J. Phys. Soc. Jpn.*, **91** (2022) 104602.
16) Y. Sakabe, N. Wada, and Y. Hamaji: *J. Korean Phys. Soc.*, **32**(1998) 260–264.
17) J.-H. Park, D. H. Yoo, C. S. Kim, H.-S. Yang, B. K. Moon, G.-J. Jung, E. D. Jeon, and K. S. Hong, Synthesis: *J. Korean Phys. Soc.*, **49**(2006) 680–683.
18) I.-H. Chu, H. Nguyen, S. Hy, Y.-C. Lin, Z. Wang, Z. Xu, Z. Deng, Y. S. Meng, and S. P. Ong: *ACS Appl. Mater. Interfaces,* **8**(2016), 7843–7853.
19) T. Baba and Y. Kawamura: *Front. Energy Res.*, **4**(2016) https://doi.org/10.3389/fenrg.2016.00022.
20) H. Stöffler, T. Zinkevich, M. Yavuz, A. Senyshyn, J. Kulisch, P. Hartmann, T. Adermann, S. Randau, F. H. Richter, J. Janek, S. Indris, and H. Ehrenberg: *J. Phys. Chem. C.*, **122**(2018) 15954–15965.
21) J. R. Dahn, R. Fong, and M. J. Spoon: *Phys. Rev. B.*, **42**(1990) 6424–6432.

22) T. Ohzuku, Y. Iwakoshi, and K. Sawai: *J. Electrochem. Soc.*, **140**(1993) 2490–2498.
23) M. K. Song, S. D. Hong, and K. T. No: *J. Electrochem. Soc.*, **148**(2001) A1159.
24) C. Sole, N. E. Drewett, and L. J. Hardwick: *Faraday Discuss.*, **172**(2014) 223–237.
25) K. Ishidzu, Y. Oka, and T. Nakamura: *Solid State Ionics,* **288**(2016), 176–179.
26) N. Nitta, F. Wu, J. T. Lee, and G. Yushin: *Materials Today*, **18**(2015) 252–264.
27) J. Rodríguez-Carvajal, G. Rousse, C. Masquelier, and M. Hervieu: *Phys. Rev. Lett.*, **81**(1998), 4660–4663.
28) A. S. Wills, N. P. Raju, and J. E. Greedan: *Chem. Mater.*, **11**(1999), 1510–1518.
29) G. Rousse: *Electrochem. Solid-State Lett.*, **2**(1999) 6–8.
30) G. Rousse, C. Masquelier, J. Rodríguez-Carvajal, E. Elkaim, J.-P. Lauriat, and J. L. Martínez: *Chem. Mater.*, **11**(1999) 3629–3635.
31) K. Tateishi, K. Suda, D. du Boulay, N. Ishizawa, and S. Oishi: *Acta Cryst.*, E**60**(2004), i18–i21.
32) R. L. McGreevy and L. Pusztai: *Molec. Sim.*, **1**(1988), 359–367.
33) Th. Proffen and S. J. L. Billinge: *J. Appl. Cryst.*, **32**(1999), 572–575.
34) V. M. Nield, D. A. Keen, W. Hayes, and R. L. McGreevy: *J. Phys.*: *Condens. Matter.*, **4**(1992) 6703–6714.
35) A. Mellergård and R. L. McGreevy: *Acta Crystallogr. A Found. Cryst.*, **55**(1999), 783–789.
36) A. Mellergård and R. L. McGreevy: *Chem. Phys.,* **261**(2000), 267–274.
37) M. G. Tucker, M. T. Dove, and D. A. Keen: *J. Appl. Cryst.,* **34**(2001), 630–638.
38) M. G. Tucker, D. A. Keen, M. T. Dove, A. L. Goodwin, and Q. Hui: *J. Phys.*: *Condens. Matter.,* **19**(2007), 335218.
39) K. Momma and F. Izumi: *J. Appl. Crystallogr.*, **44**(2011) 1272–1276.
40) I. D. Brown and D. Altermatt: *Acta Crystallogr. B Struct. Sci.*, **41**(1985), 244–247.
41) K. Kodama, N. Igawa, S. Shamoto, K. Ikeda, H. Oshita, N. Kaneko, T. Otomo, and K. Suzuya: *J. Phys. Soc. Jpn.*, **82**(2013), 094601.